Journal of Geophysical Research: Space Physics

RESEARCH ARTICLE
10.1029/2018JA025990

Key Points:
- Nondispersive Alfvén-wave power flowing into the cusp region from the magnetosphere deposits energy most efficiently at *F* region altitudes
- Comparatively little Alfvén-wave power at frequencies greater than about 0.1 Hz is deposited in the *E* region
- The *F* region Joule heating rate for Alfvénic variability is comparable to that of quasistatic variability of comparable amplitude

Supporting Information:
- Supporting Information S1
- Figure S1
- Figure S2
- Figure S3

Correspondence to:
W. Lotko,
wlotko@dartmouth.edu

Citation:
Lotko, W., & Zhang, B. (2018). Alfvénic heating in the cusp ionosphere-thermosphere. *Journal of Geophysical Research: Space Physics*, *123*, 10,368–10,383. https://doi.org/10.1029/2018JA025990

Received 10 AUG 2018
Accepted 6 DEC 2018
Accepted article online 8 DEC 2018
Published online 27 DEC 2018
Corrected 1 MAR 2019

This article was corrected on 1 MAR 2019. See the end of the full text for details.

Alfvénic Heating in the Cusp Ionosphere-Thermosphere

William Lotko[1,2] **and Binzheng Zhang**[2,3]

[1]Thayer School of Engineering, Dartmouth College, Hanover, NH, USA, [2]High Altitude Observatory, National Center for Atmospheric Research, Boulder, CO, USA, [3]Now at Laboratory for Space Research, The University of Hong Kong, Pokfulam, Hong Kong

Abstract The effect of electromagnetic variability on cusp-region ionosphere-thermosphere heating is examined. The study is motivated by observed correlations between anomalous thermospheric density enhancements at *F* region altitudes and small-scale field-aligned currents, previously interpreted as evidence of ionospheric Alfvén resonator modes. Height-integrated and height-dependent heating rates for Alfvén waves incident from the magnetosphere at frequencies from 0.05 to 2 Hz and perpendicular wavelengths from 0.5 to 20 km have been calculated. The velocity well in Alfvén speed surrounding the *F* region plasma density maximum facilitates energy deposition by slowing, trapping, and intensifying resonant waves. The Alfvénic Joule heating rate maximizes at the resulting resonances. *F* region Joule heating resulting from quasistatic and Alfvénic variability with the same root-mean-square amplitude in the *F* region are shown to be comparable. At the same time, Alfvénic variability deposits little electromagnetic power in the *E* region, whereas quasistatic variability greatly enhances *E* region heating. When measured electric and magnetic fields are used to constrain the amplitude and spectral content of superposed Alfvén waves incident from the magnetosphere, the calculated *F* region heating rate ranges from 5 to 10 nW/m^3.

1. Introduction

Air density anomalies were recorded by the CHAMP satellite at altitudes near 400 km during 40% of its traversals through the high-latitude, dayside thermosphere (Kervalishvili & Lühr, 2014). The measured air density is considered anomalous because it exceeds the predictions of the MSIS (mass spectrometer and incoherent scatter) empirical atmosphere model by 20% or more. Empirical atmospheric models are used to predict satellite drag and position in low-Earth orbit, so the occurrence of such anomalies can be a significant source of error in satellite orbit determination.

The locations of the high-latitude density anomalies are approximately fixed with respect to the geomagnetic pole, and their occurrence and location are thought to be controlled by the geomagnetic field (Liu et al., 2005). The anomalous density increases and moves to lower geomagnetic latitude with increasing geomagnetic activity, while retaining its basic structure (Rentz & Lühr, 2008). A premidnight anomaly also appears with increasing geomagnetic activity.

The dayside and premidnight anomalies occur near the statistical locations of the dayside (cusp) and nightside convection throats, which are known to map to magnetic reconnection sites at the magnetopause and in the magnetotail, respectively. Soft electron precipitation with suprathermal energies on the order of 100 eV is prevalent in the convection throats. This type of precipitation is due to direct entry of magnetosheath electrons in the cusp region and from electrons of ionospheric origin that are energized at intermediate altitudes by wave-particle interactions with dispersive Alfvén waves (called broadband precipitation). Soft electron precipitation heats the *F* region ionosphere and is a likely source of the observed correlation of the anomalous air density with elevated electron temperature (Kervalishvili & Lühr, 2014).

In addition to the observed correlation between electron temperature enhancements and air density enhancements, intense, small-scale magnetic fluctuations are also commonly associated with the anomalies (Kervalishvili & Lühr, 2013). The electric current densities inferred from the magnetic perturbations are intense and may exceed 1 mA/m^2 (Rother et al., 2007). However, the single point measurements of the CHAMP satellite do not actually differentiate the spatial versus temporal character of the electrical currents that produce the magnetic fluctuations nor the absolute amplitude of the currents as a function of their perpendicular (to the ambient magnetic field) length scale. The analysis of these fluctuations uses the method of Lühr et al. (1996, 2004), which assumes that they are spatial on the time scale for the satellite to traverse them.

This interpretation is valid when the wave frequency in the plasma rest frame is much less than the Doppler frequency due to spacecraft motion across the horizontal spatial structure. The measured variability may be further interpreted as *quasistatic*, or effectively independent of time, when the time variation (inverse wave frequency in plasma rest frame) is much slower than the transit time of an Alfvén wave between the ionosphere and the high-altitude dynamo sustaining the variability. The quasistatic assumption is often invoked to perform equipotential mapping of electric fields along the geomagnetic field. As will be shown here, the intrinsic time variation of nonequipotential electric and magnetic fields is likely to be important in ionosphere-thermosphere (IT) heating at the altitudes of CHAMP measurements.

To assess a possible connection between fluctuating fields and air density anomalies, Brinkman et al. (2016) calculated Joule heating rates when a static, zero-mean, root-mean-square (*rms* or square root of the mean square) electric field is superposed on a static, uniform (dc) electric field. Their treatment was motivated in part by an accumulating body of work indicating that the contribution of electric field fluctuations to the Joule heating of the thermosphere can dominate Joule heating from large-scale convection (e.g., Codrescu et al., 1995; Matsuo & Richmond, 2008). Since both the dc and fluctuating components of the electric field are treated as quasistatic by Brinkman et al., the heating rate in the *E* region is very large in their calculation. *F* region heating, while an order of magnitude smaller, is sufficient to produce model anomalies with characteristics resembling observed anomalies when the *F* region Pedersen conductivity is simultaneously enhanced by soft electron precipitation. This behavior also occurs in global simulations of the magnetosphere-IT interaction (Zhang et al., 2012; Zhang, Varney, et al., 2015) and in regional simulations of the IT interaction (Deng et al., 2013). IT simulations without enhanced soft electron precipitation produce cusp-region air density anomalies when the geocentric solar equatorial *y* component of the interplanetary magnetic field is very intense (Crowley et al., 2010). In analyzing the frequency dependence of the Pedersen conductivity, Verkhoglyadova et al. (2018) found that relatively high-frequency (5 Hz) Alfvén waves can enhance stormtime energy deposition in the *E* and bottomside *F* region at high latitudes, up to 30% over that deduced from static electric fields. All of these studies consider relatively strong interplanetary driving and/or relatively intense precipitation.

What produces large density anomalies when ambient conditions or interplanetary driving are not exceptional? Vertical friction between the neutral gas and ion upflows induced by direct electron heating from precipitating electrons produces only a small increase (1%) in the thermospheric density at CHAMP satellite altitudes (Sadler et al., 2012). In treating an idealized initial-boundary value problem, Tu et al. (2011) found that strong *E* region heating is accompanied by a transient peak in the heating rate at *F* region altitudes when convection is suddenly switched-on at 1,000-km altitude. The sudden change evidently stimulates dissipating Alfvén waves that bounce between the highly conducting *E* layer and their reflecting, convection boundary condition imposed at 1,000 km.

Observations from the Polar (Keiling et al., 2003) and FAST (Chaston et al., 2003, 2007; Hatch et al., 2017) satellites show that magnetic variability associated with intense Alfvén-wave Poynting fluxes flowing into the ionosphere are commonly observed in the statistical locations of the thermospheric density anomalies and associated bursts of small-scale field-aligned current. In fact, the previously mentioned soft electron precipitation induced by wave-particle interactions is expected in regions of Alfvénic activity (Zhang, Lotko, et al., 2015). The spectral characteristics of the kilometer-scale field-aligned currents measured by CHAMP (Rother et al., 2007) also suggest that the large-amplitudes of the small-scale currents may be due to trapping and resonant pumping of Alfvén waves in the so-called ionospheric Alfvén resonator (IAR; Trakhtengerts & Feldstein, 1984). Ishii et al. (1992) identified Alfvén wave variations in DE-2 satellite measurements of electric and magnetic fields at altitudes of ≈300 km where thermospheric anomalies appear in CHAMP and Streak satellite data (Clemmons et al., 2008) data. The Alfvénic character in the DE-2 measurements was prominent at frequencies greater than about 0.25 Hz, corresponding to perpendicular wavelengths less than about 32 km if the time variation is interpreted entirely as a Doppler shift of the satellite moving through spatial structure.

This paper reports a new mode of IT heating due to Alfvén-wave energy deposition. The mathematical model of Lysak (1999) for Alfvén-wave propagation in a continuously stratified ionosphere is adapted for this purpose. In contrast with Lysak's numerical calculations, which considered large perpendicular wavelengths (~100 km or greater), we use the model to examine heating at perpendicular wavelengths of 20 km or

less. Coupling between the shear Alfvén and compressional magnetohydrodynamic waves is negligible at these scales, and dissipation due to the finite parallel conductivity of the ionosphere can be important. The dissipation of electromagnetic power in the ionosphere for a time-dependent, periodic driver launching Alfvén waves from high altitude is considered. The driver frequency and wavelength are swept through the relevant range of interest. Ionospheric Alfvén resonator modes are excited in the *F* region ionosphere, but these are driven modes rather feedback unstable modes (Lysak, 1991; Trakhtengerts & Feldstein, 1991), which occur in regions of low ionospheric conductivity, in contrast with the high-conductivity, dayside ionosphere treated in this paper. Our results are consistent with the model calculations of Lessard and Knudsen (2001), who focused on the reflection of Alfvén waves incident on an inhomogeneous ionosphere, in a frequency-wavelength regime similar to the one considered here, and with recent multispacecraft correlation analyses showing that field-aligned current fluctuations at transverse length scales less than about 10 km with periods less than about 10 s are most likely Alfvénic (Gjerloev et al., 2011; Lühr et al., 2015; Miles et al., 2018; Pakhotin et al., 2018).

The mathematical model, its numerical implementation, and the height profiles of wave speed and Pedersen and parallel conductivities required to evaluate IT heating throughout the ionosphere are first described (section 2). A survey of the height-integrated volumetric heating rates as a function of wave frequency and perpendicular wavelength is presented along with heating rates versus altitude (section 3). A time series analysis of superposed Alfvén waves over the range of considered frequencies and perpendicular wavelengths is performed (section 4), with heating rates calculated and compared with those derived from quasistatic electric field variability. We conclude with a discussion of the potential importance of Alfvén wave heating of the ionosphere and thermosphere in interpreting CHAMP thermospheric density anomalies.

2. Methods

2.1. Shear Alfvén Wave Propagation Model

The model to be used here describes Alfvén-wave propagation through a continuously stratified ionosphere from altitudes above 90 km and up to the ion baropause (≈2,000-km altitude). The model is based on the linearized (small-wave amplitude), cold two-fluid equations for a collisional, magnetized plasma (Lysak, 1999) under the assumption that the angular wave frequency ω is much less than the gyrofrequency (Ω_s) of ion species *s*, specifically, $\omega^2 \ll \Omega_s{}^2$ and $\omega\nu_s \ll \Omega_s{}^2$, where ν_s is the collision frequency of ion species *s*.

In this paper, we focus on the absorption of Alfvén-wave power by the collisional ionosphere and thermosphere and ignore the effects of collisionless wave-particle interactions leading to transverse ion acceleration and electron parallel acceleration. Neglecting such effects requires the wavelength perpendicular to the background magnetic field ($\lambda_\perp$) to be much larger than the ion gyroradius v_s/Ω_s (v_s is the velocity of species *s*) and the electron inertial length $\lambda_e \equiv (m_e/\mu_0 e^2 n_e)^{1/2}$ given in terms of the electron mass m_e and charge *e*, plasma density n_e, and permeability of free space μ_0. The gyroradius of O^+ ions in the tail of the ion velocity distribution (at say 10 eV) is less than 58 m in the cusp region (≈75° magnetic latitude) at all altitudes below 2,000 km. The plasma density is typically $10^4/cm^3$ or greater in this region during the summer (Kitamura et al., 2009), so the electron inertial length is 53 m or smaller. The condition to neglect electron inertial effects leading to an Alfvén wave parallel electric field is $(2\pi\lambda_e/\lambda_\perp)^2 \ll 1$ or $\lambda_\perp{}^2 \gg 0.1$ km^2. We limit the analysis to $\lambda_\perp > 0.5$ km.

Following Lysak (1999), let $Q = \nabla_\perp \cdot \boldsymbol{E}_\perp$ and $M = (\nabla_\perp \times \boldsymbol{E}_\perp)\cdot\hat{\boldsymbol{z}}$ represent the rotational and solenoidal components of the wave electric field, respectively; $J = (\nabla_\perp \times \mathbf{B}_\perp)\cdot\hat{\mathbf{z}}$ is the wave field-aligned current times μ_0, and B_z is the compressional component of the wave magnetic field. Here $\mathbf{E}_\perp$ and $\mathbf{B}_\perp$ are the vector components of the wave electric and magnetic field perpendicular to the geomagnetic field, taken to be vertical with $\hat{\mathbf{z}}$ pointing upward. With these variables, Lysak's equations for propagation of the coupled shear and compressional Alfvén waves in the ionosphere are

$$\left(\frac{\partial}{\partial t} + \frac{\sigma_P}{\varepsilon}\right) Q = -V^2 \frac{\partial J}{\partial z} \mp \frac{\sigma_H}{\varepsilon} M, \tag{1}$$

$$\left(\frac{\partial}{\partial t} + \frac{\sigma_P}{\varepsilon}\right) M = -V^2 \nabla^2 B_z \mp \frac{\sigma_H}{\varepsilon} Q, \tag{2}$$

$$\frac{\partial J}{\partial t} = -\frac{\partial Q}{\partial z} + \eta_{\parallel}\nabla_{\perp}^2 J, \tag{3}$$

$$\frac{\partial B_z}{\partial t} = -M. \tag{4}$$

Parameters appearing in (1)–(4) include the magnetic diffusivity, $\eta_{||} = 1/\mu_0\sigma_0$, the Pedersen, Hall, and parallel conductivities

$$\sigma_P = \Sigma_s \frac{n_s q_s^2}{m_s} \frac{\nu_s}{\nu_s^2 + \Omega_s^2}, \tag{5}$$

$$\sigma_H = -\Sigma_s \frac{n_s q_s^2}{m_s} \frac{\Omega_s}{\nu_s^2 + \Omega_s^2}, \tag{6}$$

$$\sigma_0 = n_e e^2 \left(\frac{1}{m_e \nu_e} + \Sigma_s \frac{1}{m_s \nu_s} \right), \tag{7}$$

the dielectric constant

$$\varepsilon = \varepsilon_0 \left(1 + \Sigma_s \frac{\omega_{ps}^2}{\nu_s^2 + \Omega_s^2} \right), \tag{8}$$

and the wave speed $V = c(\varepsilon_0/\varepsilon)^{1/2}$ in terms of the speed of light in vacuum (c) and the permittivity of free space (ε_0). In (5)–(8), n_s, q_s, m_s, and ω_{ps} are, respectively, the number density, charge, the mass, and plasma frequency of species s.

We treat the dependent variables in (1)–(4) as periodic in the vector spatial variable $\mathbf{x}_\perp$ perpendicular to the geomagnetic field, idealized as straight and uniform (more about this treatment in section 2.3). We will solve for the Fourier amplitudes $\widetilde{F}(\mathbf{k}_\perp, z, t)$ such that $F(\mathbf{x}_\perp, z, t) = \Sigma_{\mathbf{k}_\perp} \widetilde{F}(\mathbf{k}_\perp, z, t) \cos(\mathbf{k}_\perp \cdot \mathbf{x}_\perp + \phi_k)$, where F is any of Q, M, J, or B_z and ϕ_k is the phase of the kth mode. With this representation, the operator $\nabla_\perp{}^2$ in (2) and (3) can be replaced by $-k_\perp{}^2$.

If we also let $\partial/\partial t \rightarrow i\omega$, it may be shown that the shear mode variables (Q and J) decouple from the compressional mode variables (M and B_z) when

$$k_\perp^2 \gg \mu_0 \omega \sigma_H^2 / \sigma_P. \tag{9}$$

In this case the last term in (1) may be neglected. Equations (1) and (3) alone are then sufficient to solve for Q and J.

For frequencies $f < 2$ Hz, with $\sigma_P \approx 0.2$ mS, $\sigma_H \approx 0.5$ mS, inequality (9) is satisfied when $2\pi/k_\perp$ of order 20 km or smaller. We consider this limit and solve a simplified version of (1) and (3) as

$$\left(\frac{\partial}{\partial t} + \frac{\sigma_P}{\varepsilon} \right) \widetilde{Q} = -V^2 \frac{\partial \widetilde{J}}{\partial z}, \tag{10}$$

$$\frac{\partial \widetilde{J}}{\partial t} = -\frac{\partial \widetilde{Q}}{\partial z} - k_\perp^2 \eta_{\parallel} \widetilde{J}. \tag{11}$$

We now assume 2-D sheet geometry with spatial variation in x and z only, so that $Q = \partial E_x/\partial x$ and $J = \partial B_y/\partial x$. In the Fourier domain, $\mathbf{k}_\perp = k\hat{\mathbf{x}}$ with $k = 2\pi/\lambda_\perp$; $\lambda_\perp$ is the wavelength in x. In (10) and (11), $\widetilde{Q} = ik\widetilde{E}_x$ and $\widetilde{J} = ik\widetilde{B}_y$. We may now trade the variables $\widetilde{Q}$ and $\widetilde{J}$ for the sheet electric and magnetic field variables $\widetilde{E}_x$ and $\widetilde{B}_y$ (or E_x and B_y in the spatial domain). The wave magnetic field is explicitly divergence-free in this two-dimensional geometry.

2.2. Numerical Implementation

Equations (10) and (11) have the form of a dissipative, one-dimensional wave equation with spatially varying coefficients. The Christ et al. (2002) formulation of the well-known FDTD method for solving electromagnetic

wave equations is used here. We have solved equations (1)–(6) of Christ et al. (2002) numerically on a uniform grid of cell size Δz and time step Δt. Their *update coefficients* (3)–(6) in terms of our parameters are

$$ca_i = \frac{2\varepsilon_i - \sigma_{Pi}\Delta t}{2\varepsilon_i + \sigma_{Pi}\Delta t}, \quad cb_i = -\frac{\Delta t}{\Delta z}\frac{2/\mu_0}{2\varepsilon_i + \sigma_{Pi}\Delta t},$$
$$da_i = \frac{2 - k_i^2\eta_{\parallel i}\Delta t}{2 + k_i^2\eta_{\parallel i}\Delta t}, \quad db_i = -\frac{\Delta t}{\Delta z}\frac{2}{2 + k_i^2\eta_{\parallel i}\Delta t}. \tag{12}$$

Our implementation calculates the magnetic flux density B rather than the magnetic intensity H as in Christ et al. Subscript i indicates the parameter value in the ith cell. (The wavenumber k_i in the ith cell is defined in section 2.3.) The so-called Mur absorbing boundary conditions (Mur, 1981) are implemented so that the wave is transmitted without reflection at the boundaries. With definitions (12) and the Mur boundary conditions, numerical solution of equations (1) and (2) of Christ et al. is very straightforward.

The numerical domain extends from the surface of the Earth to 5,000-km altitude. The domain between 2,000- to 5,000-km altitude is a buffer region where the wave speed and Pedersen conductivity are uniform, and the coefficients (12) in the FDTD solver are constant. The wave driver described below is located in the buffer region at 4,500-km altitude, and power reflected by the stratified collisional ionosphere below is monitored above the driver at 4,750-km altitude. We verify that only upgoing power flows between the driver and the top boundary and that no power is reflected downward at the top boundary. The cell size $\Delta z = 2$ km. The time step $\Delta t = \Delta z/\max(V)$. V is the nonuniform wave speed given in section 2.1.

The system is driven periodically in time with frequency $f = \omega/2\pi$ at cell 2250 corresponding to $z_d = 4{,}500$-km altitude. The fixed amplitude electric and magnetic fields at the location of the driver at time step t^n have the form

$$E_x(z_d, t^n) = E_x\left(z_d, t^{n-1}\right) + E_0(V(z_d)\Delta t/\Delta z)\sin(\omega t^n),$$
$$B_y(z_d, t^n) = B_y(z_d, t^{n-1}) - E_0(\Delta t/\Delta z)\sin(\omega t^n). \tag{13}$$

This specification stimulates only a downward propagating Alfvén wave (180° phase difference when spatial variable z increases with altitude and background magnetic field points downward). The driver amplitude E_0 is adjustable and may be constrained by measurements for events of interest (section 4). The other factors multiplying the sinusoid ensure that the amplitude of the downward propagating wave stimulated at 4,500-km altitude is the same at each time step. An upward propagating wave is stimulated when the downward propagating wave is reflected (or partially reflected) by the inhomogeneous ionosphere below. Energy conservation requires the sum of the power dissipated in the collisional ionosphere, the reflected power monitored at an altitude above the driver, and the power transmitted through the ionosphere be equal to the power supplied by the driver: ${E_0}^2/\mu_0 V(z_d)$. The transmitted power is negligible for the profiles of background parameters described in the next section. We have verified that the error in energy conservation is $<1\%$ when the transmitted power is neglected.

When the stimulated wave interacts with the dissipative, inhomogeneous ionosphere, it takes one or more periods of the driver to achieve a replicable sinusoidal state. The diagnostics presented in sections 3 and 4 for each frequency of the driver are produced when the following convergence criteria are satisfied: The difference in amplitude between successive driver cycles of the height-integrated Joule dissipation, the height-integrated Ohmic dissipation, and the reflected power (monitored above the driver) must each be independently <0.0001. (Each of these power quantities is normalized to the power supplied by the driver.) The driver frequency is swept through $0.05\ \text{Hz} \le f \le 2\ \text{Hz}$ in steps of 0.05 Hz. The wavenumber varies from $0.05/\text{km} \le k/2\pi \le 2/\text{km}$ in steps of 0.05/km.

2.3. Ionospheric Stratification

Lysak's (1999) derivation of (1)–(4) neglects background spatial variations perpendicular to the geomagnetic field. This assumption requires the perpendicular wavelength to be much less than the length scale of perpendicular inhomogeneities of the ionosphere. As discussed in section 2.1, ignoring the coupling between

the shear and compressional modes requires $\lambda_\perp \lesssim 20$ km, so the analysis is applicable when the length scale for transverse variations in background parameters exceeds about 100 km.

For mathematical simplicity, the geomagnetic field (B_0) is treated as straight and uniform (making it also divergence-free), and the effects of its actual variation with radial distance are included in other ways. For an Alfvén wave propagating from 2,000- to 90-km altitude at the nominal magnetic latitude of the cusp (75°), dipole magnetic geometry introduces the following effects: (i) The magnetic field increases by 2.2, which increases the speed of propagation; (ii) the flux tube convergence reduces the perpendicular length scale of the wave structure by a factor of 0.59; and (iii) the field line curvature shifts the geographic location of the magnetic foot point to higher latitude by about 2°. Effect (i) is small compared to the change in wave speed due the height variation in mass density and can be considered incorporated into the vertical variation of the wave speed. Effect (ii) tends to reduce the Joule heating rate and increase the Ohmic heating rate, in going from high to low altitude. The small effect (iii) has no practical consequence for the results in the next sections, other than the interpretation of the geographic latitude of occurrence.

To include effect (ii) in the Alfvén wave solution, let B_d represent the actual spatially varying magnetic field (e.g., dipole), and note that $B_d\lambda_\perp^2 \approx$ constant for Alfvén wave propagation over the altitude range of interest. Near 75° magnetic latitude, $B_d = B_{ref}\,(r_{ref}/r)^3$ to a good approximation where $r = 1\ R_E + z$ is the geocentric radial distance, z is the altitude or height, and subscript "ref" indicates reference distance. The choice of reference distance is arbitrary. In presenting the subsequent numerical results we have chosen z_{ref} = 400 km with $r_{ref} \equiv r_{400} = 1\ R_E + 400$ km = 6,800 km, so that $\lambda_\perp(r) = \lambda_{400}(r/r_{400})^{3/2}$ with λ_{400} representing the perpendicular wavelength at z_{ref}. Thus, the height (or radial) dependence of the magnetic diffusion term on the right side of (11) includes a contribution from both $\eta_{||}(r)$ and $k^2(r) = k_{400}^2(r_{400}/r)^3 = (2\pi/\lambda_{400})^2(r_{400}/r)^3$. In subsequent numerical calculations we absorb the height dependence of the effective wavelength into an effective magnetic diffusivity defined as $\eta_{||,eff}(z) \equiv (r_{400}/(R_E + z))^3/\mu_0\sigma_0(z)$. With this definition, the solutions presented in the next section are parameterized by the perpendicular wavelength at 400-km altitude.

In a more realistic magnetic geometry with perpendicular inhomogeneities of the ambient medium, we would need to abandon the concept of perpendicular wavelength and describe the subsequent results in terms of the perpendicular length scale of the driver. Since the group velocity of nondispersive Alfvén waves is exactly magnetic field aligned, the results would be similar to those presented here, but effects such as phase mixing of wave characteristics would make the dynamics fully two-dimensional, thereby mixing perpendicular evolution in the wave parallel propagation and dynamics.

Computing a solution to equations (10) and (11) requires specification of the height profiles $\sigma_P(z)$, $\sigma_0(z)$, or $\eta_{||}(z)$ and either $V(z)$ or $\varepsilon(z)$. We used the height profiles for $\sigma_P(z)$ and $V(z)$ given by Lysak (1999) for dayside solar maximum conditions (his Figures 1a and 2a, respectively). He treated large perpendicular wavelength modes, for which the parallel conductivity and magnetic diffusivity were not needed nor given. We use the profile for σ_0 from 100- to 1,000-km altitude given by Hanson (1965) for dayside, solar maximum conditions (his Figure 2–13), linear-log extrapolated from 1,000- to 5,000-km altitude. For σ_0 at altitudes from 10 to 90 km, we used the height profiles from Reid (1979), his Figure 6b. Below 10-km altitude σ_0 is set to its value at 10 km. The altitudes profiles for $V(z)$, $\sigma_P(z)$, $\sigma_0(z)$, and $\eta_{||}(z) = 1/\mu_0\sigma_0(z)$ used in our calculations are shown in Figure 1. The dashed line (lower left panel) shows the effective $\eta_{||,eff}(z)$ including the height-dependent scale factor for the perpendicular wavelength as described above. At altitudes above 2,000 km, $V(z)$ and $\sigma_P(z)$ are constant and equal their values at 2,000-km altitude. To achieve the convergence criteria given in section 2.2, it was necessary to extrapolate $\sigma_0(z)$ above 2,000 km rather than setting it equal to its value at 2,000 km.

3. Survey of Volumetric Heating Rates

3.1. Height-Integrated Heating Rates

Ohmic ($\eta_\parallel k^2 B_y^2/\mu_0$)and Joule ($\sigma_P E_x^2$) heating rates, integrated from 0- to 2,000-km altitude, have been calculated from solutions to equations (10) and (11). The rms values over one periodic cycle of the driver (13), as a fraction of the rms Poynting flux stimulated by the driver, are shown in Figure 2 as functions of λ_{400} ranging from 0.5 to 20 km and driving frequency from 0.05 to 2 Hz. The total fractional energy absorbed (Joule

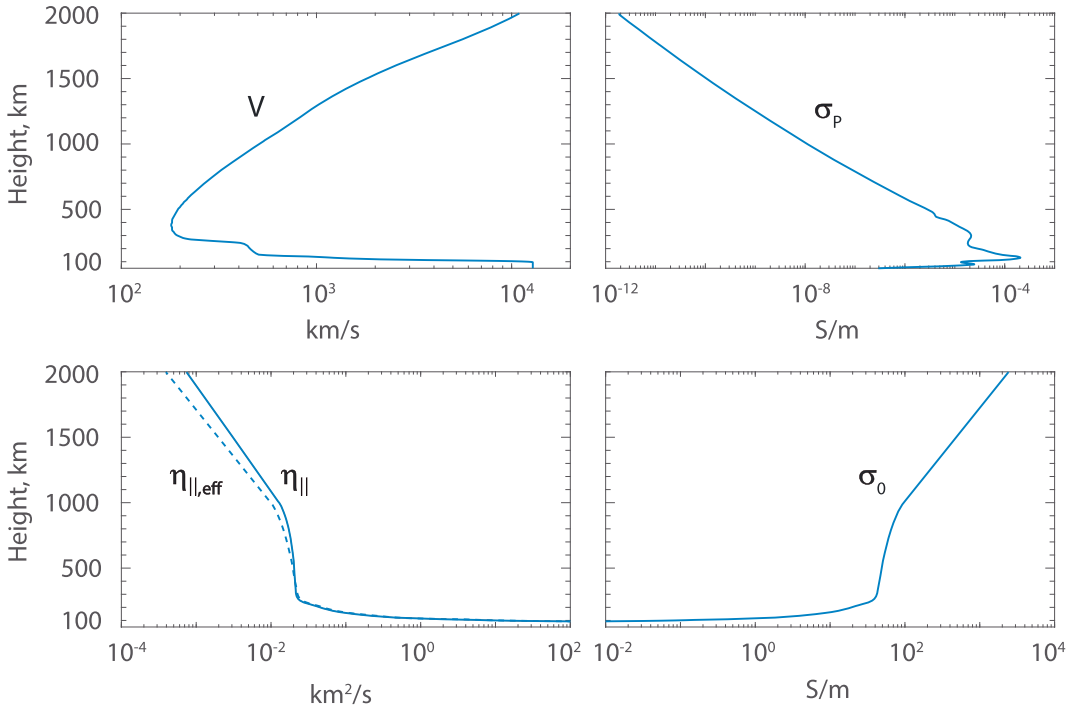

Figure 1. Height profiles of ionospheric parameters: Wave speed (*V*), Pedersen conductivity (σ_P), parallel conductivity (σ_0), and magnetic diffusivity ($\eta_{||} = 1/\mu_0\sigma_0$). The dashed line in bottom left panel is the effective $\eta_{||,eff}$ including the height-dependent scale factor for the perpendicular wavelength.

plus Ohmic) and the reflected power leaving the system through the upper boundary are also shown in Figure 2.

Absorption of dispersive wave power at $\lambda_{400} < 0.5$ km occurs at altitudes above our region of interest (i.e., above 2,000 km). This absorption (which we do not treat) is due to wave-particle interactions with electrons, and it produces the soft (broadband) electron precipitation mentioned in the introduction.

The Ohmic heating rate is significant only at the smallest wavelengths due to its $\lambda_\perp^{-2}$ dependence. As discussed below in the context of Figures 3 and 4, Ohmic dissipation absorbs the wave power in the topside ionosphere at length scales $\lambda_{400} \approx 0.5$–2 km before Joule dissipation (which tends to maximize at lower altitudes) has an opportunity to act. For $\lambda_{400} > 5$ km the height-integrated Ohmic heating rate is negligible compared to the height-integrated Joule heating rate. In this wavelength regime, the Joule heating rate appears to saturate as λ_{400} increases beyond ≈5 km. This behavior is expected at larger $\lambda_\perp$, wherein the Ohmic heating term in (11) becomes negligible, rendering the equation set in (10) and (11) independent of $\lambda_\perp$ (and $\mathbf{x}_\perp$). However, the neglected coupled shear/compressional mode equations (1)–(4) include an additional dependence on perpendicular length scale, in the first term on right side of (2). The Joule heating rate may behave differently as λ_{400} increases beyond ≈20 km, wherein shear/compressional mode coupling occurs.

The height-integrated Joule and Ohmic heating rates increase with increasing frequency of the driver in Figure 2. As shown in the next section, this behavior is due in part to the excitation of higher harmonic structure over a larger range of altitudes in the IAR. The practical upper limit on the frequency of Alfvén waves stimulated near the dayside magnetopause is probably close to 2 Hz, above which power in the driver is locally absorbed there by ion cyclotron resonance interactions (Stawarz et al., 2016). Unless some other process generates higher frequency Alfvén waves at lower altitudes, where the ion gyrofrequency is higher, one would not expect to observe appreciable Alfvén wave power propagating downward at frequencies above 2 Hz in the plasma rest frame.

Harmonic structure in the Joule heating rate (and total absorbed and reflected power) is apparent in its frequency dependence in Figure 2. Fourteen harmonics are evident with the fundamental mode at a frequency near 0.2 Hz. This harmonic structure is a consequence of the IAR, which facilitates absorption of Alfvénic

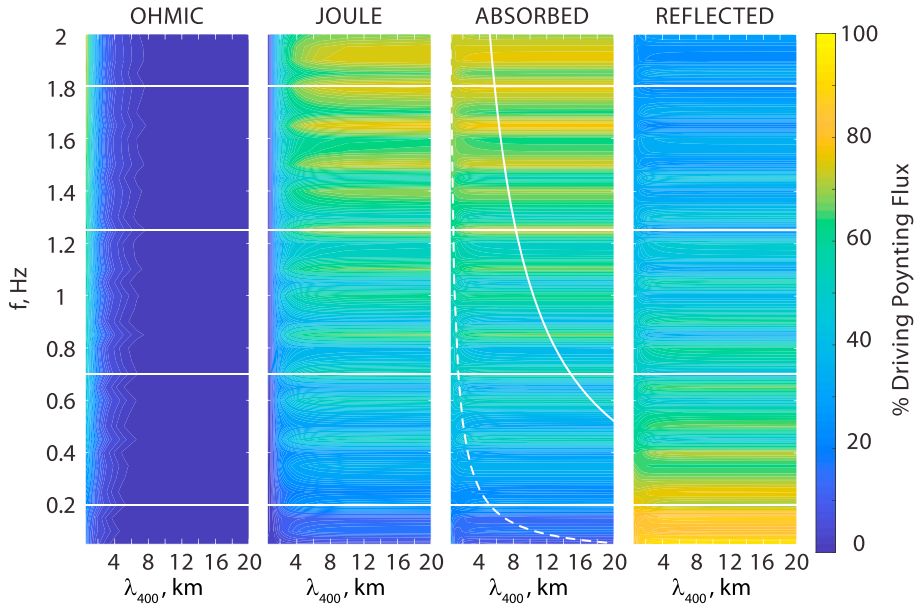

Figure 2. From left to right, rms Ohmic and Joule heating rates integrated from 0- to 2,000-km altitude as a percent of the rms (incident) Poynting flux launched by the driver vs. perpendicular wavelength at 400-km altitude (0.5 to 20 km) and driving frequency (0.05 to 2 Hz); height-integrated, rms fractional power absorbed (Joule plus Ohmic); and rms fractional reflected power leaving the system through the upper boundary. The solid (dashed) curve superposed on absorbed power delineates a satellite Doppler frequency of V_s/λ_{400} and 0.1 V_s/λ_{400} when V_s = 7.6 km/s. The altitude profiles shown in Figures 3 and 4 are sampled at the four horizontal white lines at f = 0.2, 0.7, 1.25, and 1.8 Hz in this figure.

power at the resonant frequencies. The resonant frequencies are determined by the particular profile of background Alfvén speed (Figure 1), which varies with magnetic local time, season and geomagnetic activity. The harmonic structure is not as obvious in the Ohmic heating rate, but it is also present there because the total absorption rate increases at the harmonic, indicating that harmonic Ohmic heating adds to the harmonic Joule heating.

The reflected power exhibits minima at the harmonics of the absorbed power and vice versa. The reflected power is largest at the lowest frequencies considered. These ultralow frequency Alfvén waves penetrate to the *E* region (cf. Figures 3 and 4) where most of their power is reflected.

To illustrate a potential shortcoming of assuming measured electromagnetic variability in this frequency and wavelength regime is due to Doppler shift from satellite motion through spatial structures varying slowly in time, we have superposed in the third panel curves for a satellite Doppler frequency of V_s/λ_{400} (solid white line) and 0.1 V_s/λ_{400} (dashed white line) when V_s = 7.6 km/s, the nominal speed of the CHAMP satellite at 400-km altitude. The spatial Doppler interpretation is reasonably well satisfied in the regime below the dashed curve and questionable in the regime above it. Thus, very little of the frequency-wavelength space sampled here can be considered as Doppler-shifted spatial structure at 400-km altitude where the satellite velocity is V_s = 7.6 km/s.

3.2. Height Profiles of Heating Rates

Figures 3 and 4 show the volumetric, rms Joule and Ohmic heating rates, respectively, as functions of altitude and λ_{400} for the frequencies marked by the four horizontal white lines in Figure 2 (f = 0.2, 0.7, 1.25, and 1.8 Hz). These frequency slices occur at harmonic maxima in the heating rates of Figure 2. The heating rates are normalized to the driving rms Poynting flux. We integrated the heating rates over λ_{400} so as to emphasize the altitude variation of the harmonic structure. For sinusoidal E_x and $j_{||}$, the λ_{400} integration = heating rate × ½ λ_{400}, which artificially increases the heating rate at large λ_{400} relative to that at small λ_{400}.

The fundamental mode ($f \approx$ 0.2 Hz) of the IAR exhibits a single broad maximum in the Joule heating rate at *F* region altitudes (left panel of Figure 3). The lowest altitude peak in all panels of Figure 3 occurs in the *E* layer.

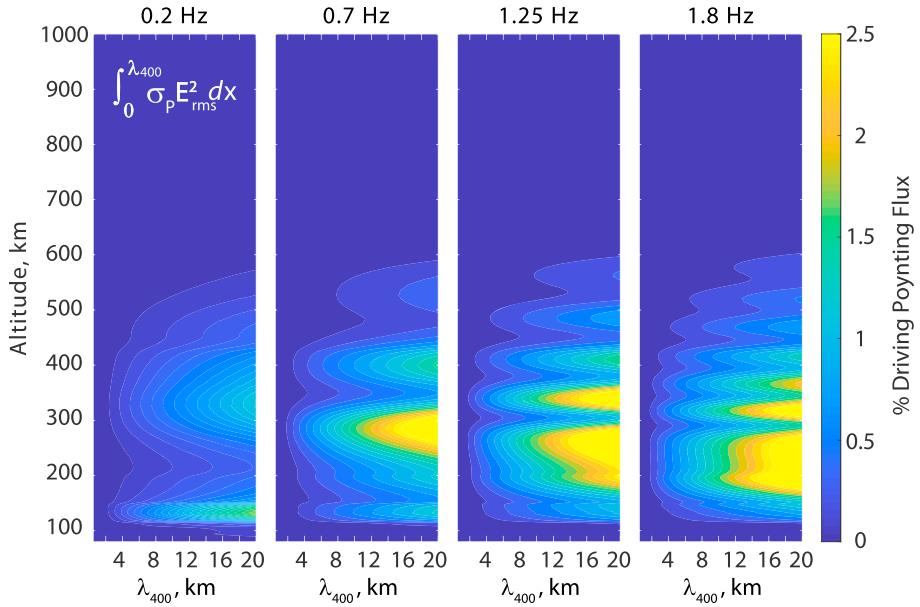

Figure 3. rms Joule heating rate integrated over λ_{400} in % of rms incident Poynting flux vs. λ_{400} and altitude (80–1,000 km).

The spatial structure in the height profiles of harmonics 5, 9 and 13, corresponding to $f = 0.7$, 1.25, and 1.8 Hz, is missing higher altitude, spatial harmonic structure. The IAR is lossier at higher altitude where the vertical gradient in wave speed (Figure 1) is more gradual, which is probably responsible for the weak or absent harmonic structure at higher altitudes.

Comparing the Joule heating rates across the four panels of Figure 3, one sees that the altitude of maximal heating depends on frequency in a complicated manner. The resonant structure in the heating rates moves to lower altitude as more IAR harmonics are excited (compare the progression from left to right in Figure 3). The heating rate is maximal in the *E* region, where σ_P maximizes, only at the lowest of the four frequencies considered ($f = 0.2$ Hz). Even in this case, the height-integrated rate is dominated by IAR harmonic heating,

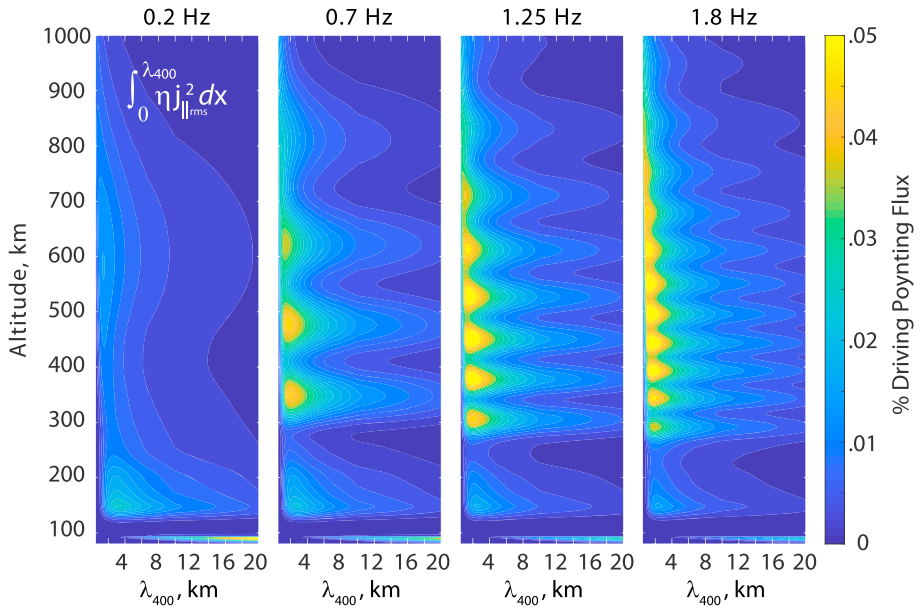

Figure 4. Same format as Figure 3 for rms integrated Ohmic heating rate with peak color-intensity 1/50 less.

which extends over a broader altitude range in the *F* region. At the higher harmonics in Figure 3, *E* region heating is clearly weaker than the *F* region heating. *E* region Joule heating is very weak at 1.25 Hz and is masked in the 1.8 Hz plot by the intense broad peak in IAR absorption near 220-km altitude.

F region Joule heating is larger than *E* region Joule heating over most of the frequency spectrum considered and is due primarily to the deep minimum in Alfvén speed near the *F* region density peak where most of the incident power is confined. This behavior is quite different from that of dc or quasistatic Joule heating which maximizes where σ_P maximizes. The intense resonant heating is due to the resonant pumping of the wave power at the resonator harmonics and to the slow wave speed in the *F* region, which causes the wave to dwell in the *F* region for a comparatively long time (e.g., compared to the dwell time in the *E* region) while its energy is absorbed.

The volumetric Ohmic heating rates shown in Figure 4 also exhibit IAR harmonic structure in the vertical profile. The factor of 50 reduction in the color scale relative to Figure 3 indicates that the Ohmic heating rates of Figure 4 are significantly smaller than Joule heating rates; but they are sustained over a greater altitude range, making the height-integrated Ohmic heating rate at small wavelengths non negligible as illustrated in Figure 2. *F* region Ohmic heating rates peak at higher altitudes than Joule heating rates where the field-aligned current remains relatively large. The field-aligned current is increasingly diverted into Pedersen current as the wave propagates to lower altitude. Since the Ohmic heating rate is proportional to $j_{||}^2$, its value is diminished at lower altitude. *E* region Ohmic heating is highest at the lowest frequencies considered.

4. Data-Constrained Heating Rate

The survey results can be used to estimate the altitude dependence of IT heating rates, with wave properties constrained by CHAMP measurements of magnetic fields and field-aligned currents and DE-2 measurements of electric and magnetic fields. For purposes of quantifying the potential significance of Alfvénic heating in IT processes, we present some preliminary results of a more comprehensive survey to come.

The time series observed at low altitude, for example, by the CHAMP satellite, must depend on how the Alfvén waves are generated at high altitude. For Alfvénic power generated by quasiperiodic solar wind variability or surface waves near the magnetopause, for example, Kelvin-Helmholtz waves, the low-altitude variability might be represented as a superposition of time-periodic Alfvén waves. Impulsive bursts of Alfvénic power might be produced by impulsive reconnection at the dayside magnetopause. Differences in the resulting low-altitude time series deserve a more extensive investigation than can be examined in this paper. As a first step, we represent the low-altitude time series of electric and magnetic fields and field-aligned current as a superposition of time-periodic Alfvén waves.

The discrete Fourier series of Alfvén waves at any given altitude *z* in the model ionosphere is given as

$$B_y(x,z,t) = \sum_{m=1}^{40}\sum_{n=1}^{40} B_{m,n}(z)\cos(2\pi mx/\lambda_{\max} + \theta_m)\cos\left(2\pi nt/\tau_{\max} + \theta_n + \phi_{m,n}\right). \tag{14}$$

Here $B_{m,n}(z)$ is the Fourier amplitude of the *m*th wavenumber and *n*th frequency mode; $\lambda_{\max}$ = 20 km is the maximum perpendicular wavelength at 400-km altitude (λ_{400}). Similarly, $\tau_{\max}$ = 20 s. Lacking knowledge of phase relationships between modes, we assign a random phase (θ_m, θ_n) for each mode relative to the others. The double sums include all 40 × 40 modes shown in Figure 2 from f = 0.05 Hz to 2 Hz and $k_{400}/2\pi$ = 0.05 to 2 km^{-1}. $\phi_{m,n}(z)$ is the phase difference between E_x and B_y for each mode (see the supporting information for illustrative plots). The electric field E_x has a similar form with the same random phases but without the phase shift $\phi_{m,n}$. The relative amplitudes of $E_{m,n}(z)$ and $B_{m,n}(z)$ satisfy the calculated local conductance relationships (see the supporting information for illustrative plots). The field-aligned current j_z is calculated from $\mu_0^{-1}\partial/\partial x$ operating on (14).

The CHAMP event described in Figure 2 of Rother et al. (2007) exhibits peak-to-peak field-aligned currents exceeding 640 μA/m^2 at 50 MHz sampling at a nominal altitude of 400 km. Such events are evidently relatively common in the CHAMP data set. Events as large as 2 mA/m^2 have also been reported (Rother et al., 2007), in Ørsted satellite measurements as well (Neubert & Christiansen, 2003). The small-scale Alfvén-wave event in Figure 1 of Ishii et al. (1992) recorded near 300-km altitude at 10:21 UT exhibits a peak-to-peak

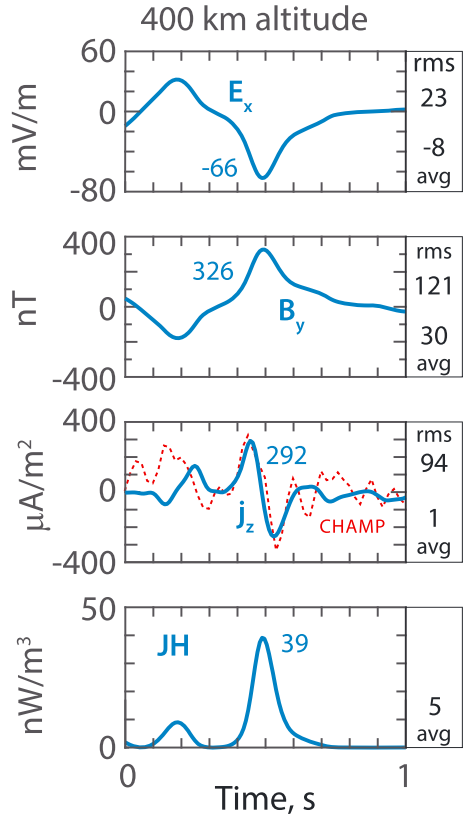

Figure 5. A 1-s interval at 400-km altitude in the time series of the electric (E_x) and magnetic (B_y) fields, field-aligned current (j_z), and Joule heating rate (JH) of superposed Alfvén waves calculated from (14) for one realization of random phases ($\theta_{m,n}$). Peak values are labeled in each panel, with rms (top number) and average (bottom) values in boxes to the right. The red curve for j_z is extracted from a CHAMP time series (Figure 2 of Rother et al., 2007).

magnetic fluctuation of 390 nT and a peak-to-peak electric fluctuation exceeding 80 mV/m. In our analysis, the Alfvénic electric and magnetic fields are even larger at the CHAMP altitude than at the 300-km altitude of the DE-2 event. We use these nominal values to constrain the approximate amplitudes of electric and magnetic fields and field-aligned currents in a model calculation.

The amplitude spectra of field-aligned currents shown in Figure 3 of Rother et al. (2007) exhibit modest variation (almost flat) with frequency between 0.1 and 9 Hz and roll-off exponentially beyond 10 Hz. The satellite Doppler effect is accommodated in (14) by setting the horizontal coordinate $x = V_s t$, where V_s = 7.6 km/s is the presumed satellite velocity (the nominal CHAMP satellite velocity at 400-km altitude). Thus, at a given altitude (constant z coordinate), the superposed Fourier mode representation of the field-aligned current derived from (14) becomes a function of time only. Intrinsic (plasma rest frame) time variation of the modeled Alfvén wave fields occurs for frequencies 0.05 Hz $\leq f \leq$ 2 Hz (cf. discussion in section 3.1), while the Doppler effect at 400-km altitude contributes to apparent time variation at frequencies 0.4 Hz $< V_s/\lambda_{400} <$ 15 Hz. It is not known from in situ satellite observations how much of the Alfvén frequency spectrum is due to intrinsic time variation versus the Doppler effect or how many wave modes are active in actual events. Thus, the model field represented by (14) may be a plausible model for the observed fields, but it likely differs in harmonic content from actual measured fields.

The fields calculated from (14) for B_y and similar series for E_x and j_z with $x = V_s t$ at the nominal CHAMP altitude of z = 400 km are shown in Figure 5 for a 1-s interval contained within a longer 26.3 s time series (see Figure S3 in the supporting information), corresponding to a 200-km transect along the satellite orbit (mean width of such events in the CHAMP data). The time series was generated by the realization of the random phases $\theta_{m,n}$ in (14) given in the supporting information. The amplitudes of all m,n modes in the Alfvén wave expansion for $j_z \propto (2\pi m/\lambda_{max})B_{m,n}(z)$ are set to the same constant value, which yields a flat amplitude spectrum (not shown) in the frequency domain out to about 8 Hz with an exponential roll-off at higher Doppler frequencies, as in Figure 3 of Rother et al. (2007). With this specification for j_z, the amplitudes $B_{m,n}(z)$ and $E_{m,n}(z)$ are proportional to $\lambda_{max}/2\pi m$.

The amplitude of the high-altitude electric field driver, E_0 in (13), used to produce the time series was scaled to 12 mV/m to yield low-altitude peak electric (E_x) and magnetic (B_y) fields and field-aligned current (j_z) representative of CHAMP and DE-2 measurements. The 12 mV/m driver required to produce the fields in Figure 5 is not necessarily representative of measured electric fields at the driving altitude (4,500 km), since the background magnetic field and Alfvén speed are unrealistically uniform above 2,000 km. Field variations due magnetic lensing in the converging the flux tube and partial reflections of the wave field from continuously varying field-aligned gradients in the wave speed are absent in the uniform region at altitudes above 2,000 km. We consider the high-altitude driver simply to be a vehicle for launching Alfvén waves that propagate into the ionosphere, with amplitude adjusted so as to model observed fields at ionospheric altitudes.

Details of the time series in Figure 5 are similar to the small-scale structure resolved by 50 Hz sampling in CHAMP data. The 1-s interval of Figure 5 was chosen for the reversed field-aligned current structure exhibited in panel 3, which resembles in structure and amplitude an intense field-aligned current (red curve in panel 3) reported by Rother et al. (2007), their Figure 2. Our sampling is a bit coarser because it extends only to V_s/λ_{min} = 15 Hz; however, as noted above, the field-aligned currents inferred at CHAMP altitudes contain little power at frequencies above 10 Hz. The ratio of peak $|j_z|$ to rms j_z in Figure 5 is 3.1. This ratio is close to but less than the statistical regression slope of 3.75 for CHAMP field-aligned currents reported by Rother et al., their Figure 6.

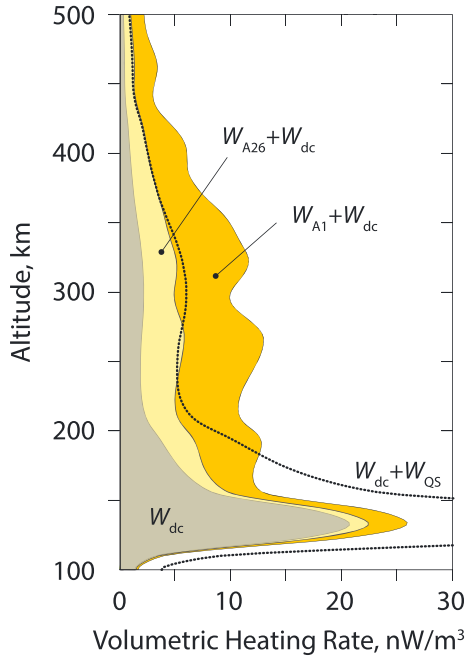

Figure 6. Height profiles of Joule heating rates for a 10-mV/m static, uniform dc electric field (W_{dc}); for the same W_{dc} added to a 1-s average of the Alfvénic Joule heating rate W_{A1} at each altitude (the 1-s interval at 400-km altitude is shown in Figure 5) and for the same W_{dc} added to an altitude-dependent, Alfvénic Joule heating rate W_{A26} averaged over a longer time series (26.3 s) from which the 1-s interval in Figure 5 was extracted. See text for explanation of the dotted curve ($W_{dc} + W_{QS}$).

Prominent features in the modeled time series of Figure 5 are similar at other altitudes, but the field amplitudes are smaller (larger) at lower (higher) altitudes. Like the sample heating rates shown in Figure 3, the Joule heating rate increases (decreases) at lower (higher) altitude due to the increase in Pedersen conductivity with decreasing altitude, but, with inclusion of 40x40 Alfvén modes in (14), the Joule heating rate of the modeled time series peaks in the lower *F* region rather than in the *E* region.

We calculated the height-dependent, Alfvénic Joule heating rate at altitudes from 100 to 500 km from time averages taken within the same 1-s time interval of Figure 5 ($W_{A1} = \sigma_P(z)\ \langle E_A^2(z)\rangle_1$) and from time averages of the complete 26.3-s time series ($W_{A26} = \sigma_P(z)\ \langle E_A^2(z)\rangle_{26}$) from which this 1-s interval is extracted. The resulting average heating rates (Figure 6) were then added to the heating rate $W_{dc} = \sigma_P(z)E_{dc}^2$ produced by a uniform dc field of 10 mV/m representing an average, large-scale convection electric field in the cusp. E_{dc} is nearly constant between 100- and 500-km altitude, so the altitude profile of W_{dc} alone in Figure 6 follows that of $\sigma_P(z)$ in Figure 1. W_{A26} is illustrative of an average profile of thermospheric heating rate across a 200-km-wide cusp, whereas W_{A1} illustrates the profile of average, high burst rate heating in a single 1-s interval. The Ohmic heating rate is not included in our calculated rates because it is small in comparison to Joule heating and because it mainly heats ions rather than neutrals at *F* region altitudes and above.

Figure 6 also shows a case when the dc Joule heating rate is added to a fictitious Joule heating rate—identified as a pseudo quasistatic (W_{QS}) rate. W_{QS} is calculated by assuming that the rms Alfvénic electric field amplitude at 400-km altitude is electrostatic rather than inductive, with the electric field at other altitudes determined by static mapping along the background magnetic field (at 100- to 500-km altitude, a quasistatic electric field, like E_{dc}, is essentially independent of *z*). The dotted curve in Figure 6 shows the resulting $W_{dc} + W_{QS}$. Its off-scale peak value of 58 nW/m^3 obtained from the 26.3-s rms average electric field occurs at 132-km altitude in the *E* region where $\sigma_P(z)$ peaks.

The combined Alfvénic plus dc heating rates also peak near the *E* region peak in $\sigma_P(z)$, with the location and magnitude of the peak controlled by the profile of W_{dc}. $W_{A26} + W_{dc}$ and $W_{A1} + W_{dc}$ exhibit secondary peaks of 5.8 nW/m^3 (26.3-s average) and 12.9 nW/m^3 (1-s average) in the *F* region at 268-km altitude. W_A alone peaks near this same altitude and then decreases at *E* region altitudes to less than one half of its peak value and to a small fraction of W_{dc}. As discussed below, this feature of Alfvénic heating can produce CHAMP thermospheric density enhancements at 400 km.

The Alfvénic heating profile ($W_A + W_{dc}$) and the pseudo quasistatic heating profile ($W_{QS} + W_{dc}$) are similar at *F* region altitudes, but they differ very significantly at *E* region altitudes. This comparison indicates that misinterpretation of inductive electric fields measured in the ionosphere can lead to estimates of anomalously high Joule heating rates in the *E* region. Given the large difference in *E* region Joule heating rates for Alfvénic and quasistatic fields, the implications of this difference for ionospheric and thermospheric energetics are significant.

We can qualify the results in Figure 6 in the context of other models of Joule heating that produce thermospheric density anomalies resembling those measured by the CHAMP satellite. Brinkman et al. (2016) examined Joule heating produced by zero-mean, quasistatic, rms electric fields of 20 and 50 mV/m added to the heating rate produced by a static, uniform convection field of E_{dc} = 10 mV/m. The altitude profiles for their combined heating rates resemble in magnitude and altitude distribution the pseudo quasistatic profile in Figure 6. Brinkman et al. note that their large volumetric Joule heating rates in the *E* region are less important for the neutral gas upwellings observed by CHAMP than the smaller *F* region rates, because the heating rate per unit mass, $\sigma_P(z)E^2/\rho_{air}(z)$, is amplified in the *F* region owing the more rapid exponential decrease of the air

density $\rho_{air}(z)$ with increasing altitude relative to the decrease in $\sigma_P(z)$. The Alfvénic heating rates calculated here give heating rates per unit mass in the *F* region comparable to those of Brinkman et al. The fact that Alfvén waves deposit energy predominantly in the *F* region makes Alfvénic heating especially important for mesoscale and small-scale heating processes that enhance the thermospheric temperature and density at *F* region altitudes and higher.

Zhang et al. (2012) and Deng et al. (2013) examined the effects of soft electron precipitation on Joule heating and thermospheric upwelling in large-scale models of the IT interaction (including also coupling to the magnetosphere in Zhang et al.'s study). Both found that the enhancement in *F* region Pedersen conductivity due to enhanced ionization from ~100-eV electron precipitation significantly augments *F* region Joule heating and thermospheric upwelling, particularly during geomagnetic storm conditions (Zhang, Lotko, et al., 2015). This result was anticipated in an earlier modeling study by Clemmons et al. (2008), and it was also included in the aforementioned study by Brinkman et al. (2016). Had the effects of soft electron precipitation been included in the conductivity profile used here, we would expect to obtain even higher *F* region Joule heating rates for Alfvénic electric fields.

We conclude that superposed Alfvénic electric fields have a minor influence on *E* region Joule heating and a comparatively large effect on *F* region Joule heating. *F* region Alfvénic Joule heating rates are comparable to those obtained from heating models based on quasistatic electric field variability, when the rms amplitude of quasistatic and Alfvénic fields near the *F* region peak are comparable. However, quasistatic variability tends to greatly enhance *E* region Joule heating relative to Alfvénic variability.

The modeled field-aligned current (j_z) in Figure 5 was computed from the curl of wave B_y with scaling of the driver amplitude chosen to give a peak value of j_z consistent with CHAMP measurements. An analysis of differences in amplitude and spectral content between model j_z when computed from the curl ($\partial/\partial x$) and from the Doppler derivative ($\partial/\partial V_s t$), as was done for the CHAMP data, should be undertaken in the future. Any significant differences may propagate through the model Joule and Ohmic heating rates.

5. Conclusions

This investigation was motivated by CHAMP satellite measurements of large anomalies in the thermospheric density correlated with intense small-scale magnetic fluctuations near the cusp and dayside convection throat at altitudes near 400 km. The magnetic fluctuations are modeled here as Alfvén waves, and the effects of Alfvén wave energy deposition on IT heating are considered. Heating rates have been calculated as a function of altitude and wave frequency and perpendicular wavelength. A future step in assessing the effects of the Alfvén-wave heating on thermosphere and ionosphere densities, temperatures, and composition requires using the heating rates in a thermosphere-ionosphere general circulation model.

Specifically, we analyzed Joule and Ohmic heating rates resulting from Alfvén waves incident from high altitude on a stratified, dayside ionosphere specified by profiles of the Alfvén speed and the Pedersen and parallel conductivities representative of the cusp region. Alfvén wave frequencies ranging from 0.05 to 2 Hz and perpendicular wavelengths at 400 km altitude from 0.5 to 20 km were considered. Electron inertial effects are negligible at wavelengths $>$0.5 km in the ionosphere, and weak coupling between the shear Alfvén and compressional modes at wavelengths $<$20 km allows effects of Alfvén-wave induced Hall currents to be neglected in the analysis. The upper value of the considered frequencies is not limited by the physical model per se. Rather, when considering likely high-altitude sources of Alfvén waves near the dayside magnetopause, power at frequencies near and above the local gyrofrequency is locally absorbed there and therefore is unlikely to stimulate appreciable power in downward propagating Alfvén waves.

The principal results of this paper include the following:

1. In contrast to heating by dc and quasistatic electric fields, which cause Joule heating primarily in the *E* region ionosphere, superposed Alfvén-wave electric fields at frequencies from 0.05 to 2 Hz and perpendicular wavelengths from 0.5 to 20 km mainly heat the *F* region ionosphere and thermosphere (Figures 3 and 6). Previous modeling studies have shown that heating at these altitudes is needed to produce observed thermospheric density anomalies at 400-km altitude (and associated depletions observed at lower altitudes). The waves penetrate most effectively to the *E* region only at the lowest frequencies

considered, but most of the Alfvén-wave power at these low frequencies is reflected and returned to the magnetosphere rather than being absorbed. Thus, Alfvén wave energy deposition heats the IT at the altitudes needed to produce the observed thermospheric anomalies without significant heating of the *E* region, as occurs for quasistatic electric fields (section 4).

2. The structure of the IAR is responsible for the large *F* region energy deposition by the waves. The classical IAR is a lossy cavity that traps Alfvén waves between the conducting *E* layer and the topside gradient in Alfvén speed. Over most of the frequency range considered here and for the model ionospheric profile, the Alfvén wave power reaching the *E* layer is weak, and the resonance structure is due primarily to the deep minimum in Alfvén speed near the *F* region density peak where most of the incident power is confined. The Joule heating rate maximizes at resonance maxima in the electric field (Figure 2) and, for a given frequency, exhibits a harmonic structure with altitude (Figure 3).
3. The Ohmic heating rate (due to the parallel resistivity of the ionosphere) is comparatively weak, with peak values about 50x smaller than those of the Joule heating rate (Figure 4). However, the Ohmic heating extends over a greater altitude range than Joule heating. At the smallest perpendicular wavelengths considered, the height-integrated Ohmic heating rate may be an important factor in topside ionospheric ion upwelling. Further investigation is needed.
4. The wave impedance ($\mu_0 E_{wave}/B_{wave}$) is Alfvénic ($\mu_0 V_A$) or nearly Alfvénic based on the local Alfvén speed throughout most of the IAR heating region (Figure S1 in the supporting information). Deviations occur in the *E* layer and for low-frequency Alfvén waves observed at higher altitude wherein the wave conductance approaches the Pedersen conductance. Thus the inferred wave conductance should provide a reasonably good diagnostic of the Alfvénic character of wave fields measured in the IAR.
5. The Joule heating rates estimated here and their variation with altitude are very different from those calculated from variable zero-mean, quasistatic fields. Alfvén waves deposit energy predominantly at resonances of the IAR, which occur mainly in the *F* region ionosphere. The waves deposit comparatively little power in the *E* region, in contrast with variable zero-mean, quasistatic fields which deposit energy predominantly in the *E* region. The *F* region Joule heating rates resulting from quasistatic and Alfvénic electric field variability are comparable when the rms amplitudes are comparable in the *F* region (section 4 and Figure 6).

This work addresses an important question regarding the nature of electric field variability inferred on polar-orbiting satellites. To what extent are observed fields quasistatic or Alfvénic? While quasistatic fields map along equipotential magnetic field lines, Alfvénic fields do not. The altitude profiles of IT heating are therefore very different for the two cases. The quasistatic assumption is typically invoked in statistical studies of low-altitude electric field variability, but the assumption may not be uniformly valid across the observed spectrum of variability.

Much work remains to determine the relative importance of Alfvén-wave heating in the ionosphere and thermosphere relative to other processes. Next steps should include the following:

1. Analysis of the differences in model time series, amplitude spectra, and heating rates when the data-constrained field-aligned current is derived from the Doppler-derivative approximation for the curl of the wave magnetic field rather than the actual curl of the wave magnetic field, as was done here.
2. Event and statistical modeling of observed *F* region time series of electric and magnetic fields, for example, as reported by Ishii et al. (1992) and Rother et al. (2007), including an evaluation of the implied heating rates.
3. Analysis of differences in heating rates derived from periodic (as was done here) versus impulsive Alfvén-wave drivers.
4. Surveys of heating rates for ambient ionospheric and thermospheric states representative of different local times, solar cycle, and activity conditions, for example, based on empirical reference models such as the International Reference Ionosphere (IRI) and MSIS models.
5. Evaluation of effects on heating rates of coupling between Alfvén and compressional magnetohydrodynamic waves, which requires treatment of Hall currents at larger perpendicular wavelengths.
6. Modeling the effects of broadband (soft) electron precipitation on the *F* region conductivity.
7. Using Alfvén-wave heating rates in a thermosphere-ionosphere general circulation model to evaluate their effects on the density, temperature and composition of the thermosphere and ionosphere.

Since Alfvén waves appear to be prevalent where thermospheric density anomalies are observed, their effects on thermospheric heating and on the formation of ion upflows in these regions merit further study.

Acknowledgments
The paper is theoretical and no data are used. All information required to reproduce the numerical results in the figures is given in the paper and in cited publications. The research was supported by the National Aeronautics and Space Administration under grant NNX14AN52G, by Thayer School of Engineering at Dartmouth College, and by the High Altitude Observatory of the National Center for Atmospheric Research.

References

Brinkman, D. G., Walterscheid, R. L., Clemmons, J. H., & Hecht, J. H. (2016). High-resolution modeling of the cusp density anomaly: Response to particle and Joule heating under typical conditions. *Journal of Geophysical Research: Space Physics*, *121*, 2645–2661. https://doi.org/10.1002/2015JA021658

Chaston, C. C., Bonnell, J. W., Carlson, C. W., McFadden, J. P., Ergun, R. E., & Strangeway, R. J. (2003). Properties of small-scale Alfvén waves and accelerated electrons from FAST. *Journal of Geophysical Research*, *108*(A4), 8003 https://doi.org/10.1029/2002JA009420

Chaston, C. C., Carlson, C. W., McFadden, J. P., Ergun, R. E., & Strangeway, R. J. (2007). How important are dispersive Alfvén waves for auroral particle acceleration? *Geophysical Research Letters*, *34*, L07101. https://doi.org/10.1029/2006GL029144

Christ, A., Frohlich, J., & Kuster, N. (2002). Correction of numerical phase velocity errors in nonuniform FDTD meshes. *IEICE Transactions on Communications*, *E85B*, 2904–2915.

Clemmons, J. H., Hecht, J. H., Salem, D. R., & Strickland, D. J. (2008). Thermospheric density in the Earth's magnetic cusp as observed by the Streak mission. *Geophysical Research Letters*, *35*, L24103. https://doi.org/10.1029/2008GL035972

Codrescu, M. V., Fuller-Rowell, T. J., & Foster, J. C. (1995). On the importance of E-field variability for Joule heating in the high-latitude thermosphere. *Geophysical Research Letters*, *22*(17), 2393–2396. https://doi.org/10.1029/95GL01909

Crowley, G., Knipp, D. J., Drake, K. A., Lei, J., Sutton, E., & Lühr, H. (2010). Thermospheric density enhancements in the dayside cusp region during strong B_Y conditions. *Geophysical Research Letters*, *37*, L07110. https://doi.org/10.1029/2009GL042143

Deng, Y., Fuller-Rowell, T. J., Ridley, A. J., Knipp, D., & Lopez, R. E. (2013). Theoretical study: Influence of different energy sources on the cusp neutral density enhancement. *Journal of Geophysical Research: Space Physics*, *118*, 2340–2349. https://doi.org/10.1002/jgra.50197

Gjerloev, J. W., Ohtani, S., Iijima, T., Anderson, B., Slavin, J., & Le, G. (2011). Characteristics of the terrestrial field-aligned current system. *Annales de Geophysique*, *29*(10), 1713–1729. https://doi.org/10.5194/angeo-29-1713-2011

Hanson, W. B. (1965). Structure of the ionosphere. In F. S. Johnson (Ed.), *Satellite environment handbook* (chap. 2, 2nd ed., pp. 23–49). Stanford University Press, Stanford, CA.

Hatch, S. M., LaBelle, J., Lotko, W., Chaston, C. C., & Zhang, B. (2017). IMF control of Alfvénic energy transport and deposition at high latitudes. *Journal of Geophysical Research: Space Physics*, *122*, 12,189–12,211. https://doi.org/10.1002/2017JA024175

Ishii, M., Sugiura, M., Iyemori, T., & Slavin, J. A. (1992). Correlation between magnetic and electric field perturbations in the field-aligned current regions deduced from DE 2 observations. *Journal of Geophysical Research*, *97*(A9), 13,877–13,887. https://doi.org/10.1029/92JA00110

Keiling, A., Wygant, J. R., Cattell, C. A., Mozer, F. S., & Russell, C. T. (2003). The global morphology of wave Poynting flux: Powering the aurora. *Science*, *299*(5605), 383–386. https://doi.org/10.1126/science.1080073

Kervalishvili, G. N., & Lühr, H. (2013). The relationship of thermospheric density anomaly with electron temperature, small-scale FAC, and ion up-flow in the cusp region, observed by CHAMP and DMSP satellites. *Annales de Geophysique*, *31*(3), 541–554. https://doi.org/10.5194/angeo-31-541-2013

Kervalishvili, G. N., & Lühr, H. (2014). Climatology of zonal wind and large-scale FAC with respect to the density anomaly in the cusp region: Seasonal, solar cycle, and IMF By dependence. *Annales de Geophysique*, *32*(3), 249–261. https://doi.org/10.5194/angeo-32-249-2014

Kitamura, N., Shinbori, A., Nishimura, Y., Ono, T., Iizima, M., & Kumamoto, A. (2009). Seasonal variations of the electron density distribution in the polar region during geomagnetically quiet periods near solar maximum. *Journal of Geophysical Research*, *114*, A01206. https://doi.org/10.1029/2008JA013288

Lessard, M. R., & Knudsen, D. J. (2001). Ionospheric reflection of small-scale Alfvén waves. *Geophysical Research Letters*, *28*(18), 3573–3576. https://doi.org/10.1029/2000GL012529

Liu, H., Lühr, H., Henize, V., & Köhler, W. (2005). Global distribution of the thermospheric total mass density derived from CHAMP. *Journal of Geophysical Research*, *110*, A04301. https://doi.org/10.1029/2004JA010741

Lühr, H., Park, J., Gjerloev, J. W., Rauberg, J., Michaelis, I., Merayo, J. M. G., & Brauer, P. (2015). Field-aligned currents' scale analysis performed with the Swarm constellation. *Geophysical Research Letters*, *42*, 1–8. https://doi.org/10.1002/2014GL062453

Lühr, H., Rother, M., Köhler, W., Ritter, P., & Grunwaldt, L. (2004). Thermospheric upwelling in the cusp region: Evidence from CHAMP observations. *Geophysical Research Letters*, *31*, L06805. https://doi.org/10.1029/2003GL019314

Lühr, H., Warnecke, J., & Rother, M. K. A. (1996). An algorithm for estimating field-aligned currents from single spacecraft magnetic field measurements: A diagnostic tool applied to Freja satellite data. *IEEE Transactions on Geoscience and Remote Sensing*, *34*(6), 1369–1376. https://doi.org/10.1109/36.544560

Lysak, R. L. (1991). Feedback instability of the ionospheric resonant cavity. *Journal of Geophysical Research*, *96*(A2), 1553–1568. https://doi.org/10.1029/90JA02154

Lysak, R. L. (1999). Propagation of Alfvén waves through the ionosphere: Dependence on ionospheric parameters. *Journal of Geophysical Research*, *104*(A5), 10,017–10,030. https://doi.org/10.1029/1999JA900024

Matsuo, T., & Richmond, A. D. (2008). Effects of high-latitude ionospheric electric field variability on global thermospheric Joule heating and mechanical energy transfer rate. *Journal of Geophysical Research*, *113*, A07309. https://doi.org/10.1029/2007JA012993

Miles, D. M., Mann, I. R., Pakhotin, I. P., Burchill, J. K., Howarth, A. D., Knudsen, D. J., Lysak, R. L., et al. (2018). Alfvénic dynamics and fine structuring of discrete auroral arcs: Swarm and e-POP observations. *Geophysical Research Letters*, *45*, 545–555. https://doi.org/10.1002/2017GL076051

Mur, G. (1981). Absorbing boundary conditions for the finite-difference approximation of the time-domain electromagnetic-field equations. *IEEE Transactions on Electromagnetic Compatibility*, *EMC-23*(4), 377–382. https://doi.org/10.1109/TEMC.1981.303970

Neubert, T., & Christiansen, F. (2003). Small-scale, field-aligned currents at the top-side ionosphere. *Geophysical Research Letters*, *30*(19), 2010. https://doi.org/10.1029/2003GL017808

Pakhotin, I. P., Mann, I. R., Lysak, R. L., Knudsen, D. J., Gjerloev, J. W., Rae, I. J., Forsyth, C., et al. (2018). Diagnosing the role of Alfvén waves in magnetosphere-ionosphere coupling: Swarm observations of large amplitude nonstationary magnetic perturbations during an interval of northward IMF. *Journal of Geophysical Research: Space Physics*, *123*, 326–340. https://doi.org/10.1002/2017JA024713

Reid, G.C. (1979). The middle atmosphere. In N. C. Maynard (Ed.), *Appendix A in Middle atmosphere electrodynamics: Report of the workshop on the role of the electrodynamics of the middle atmosphere on solar-terrestrial coupling* (pp. 27–42, Report Number NASA-CP-2090). Greenbelt, MD: NASA Goddard Space Flight Center. https://ntrs.nasa.gov/search.jsp?R=19790017437

Rentz, S., & Lühr, H. (2008). Climatology of the cusp-related thermospheric mass density anomaly, as derived from CHAMP observations. *Annales de Geophysique*, *26*(9), 2807–2823. https://doi.org/10.5194/angeo-26-2807-2008

Rother, M., Schlegel, K., & Lühr, H. (2007). CHAMP observation of intense kilometer-scale field-aligned currents, evidence for an ionospheric Alfvén resonator. *Annales de Geophysique*, *25*(7), 1603–1615. https://doi.org/10.5194/angeo-25-1603-2007

Sadler, F. B., Lessard, M., Lund, E., Otto, A., & Lühr, H. (2012). Auroral precipitation/ion upwelling as a driver of neutral density enhancement in the cusp. *Journal of Atmospheric and Solar - Terrestrial Physics*, *87-88*, 82–90. https://doi.org/10.1016/j.jastp.2012.03.003

Stawarz, J. E., Eriksson, S., Wilder, F. D., Ergun, R. E., Schwartz, S. J., Pouquet, A., Burch, J. L., et al. (2016). Observations of turbulence in a Kelvin-Helmholtz event on 8 September 2015 by the Magnetospheric Multiscale mission. *Journal of Geophysical Research: Space Physics*, *121*, 11,021–11,034. https://doi.org/10.1002/2016JA023458

Trakhtengerts, V. Y., & Feldstein, A. Y. (1984). Quiet auroral arcs: Ionosphere effect of magnet spheric convection stratification. *Planetary and Space Science*, *32*(2), 127–134. https://doi.org/10.1016/0032-0633(84)90147-8

Trakhtengerts, V. Y., & Feldstein, A. Y. (1991). Turbulent Alfvén boundary layer in the polar ionosphere: 1. Excitation conditions and energetics. *Journal of Geophysical Research*, *96*(A11), 19,363–19,374. https://doi.org/10.1029/91JA00376

Tu, J., Song, P., & Vasyliunas, V. M. (2011). Ionosphere/thermosphere heating determined from dynamic magnetosphere-ionosphere/thermosphere coupling. *Journal of Geophysical Research*, *116*, A09311. https://doi.org/10.1029/2011JA016620

Verkhoglyadova, O. P., Meng, X., Mannucci, A. J., & McGranaghan, R. M. (2018). Semianalytical estimation of energy deposition in the ionosphere by monochromatic Alfvén waves. *Journal of Geophysical Research: Space Physics*, *123*, 5210–5222. https://doi.org/10.1029/2017JA025097

Zhang, B., Lotko, W., Brambles, O., Wiltberger, M., & Lyon, J. (2015). Electron precipitation models in global magnetosphere simulations. *Journal of Geophysical Research: Space Physics*, *120*, 1035–1056. https://doi.org/10.1002/2014JA020615

Zhang, B., Lotko, W., Brambles, O., Wiltberger, M., Wang, W., Schmitt, P., & Lyon, J. (2012). Enhancement of thermospheric mass density by soft electron precipitation. *Geophysical Research Letters*, *39*, L20102. https://doi.org/10.1029/2012GL053519

Zhang, B., Varney, R. H., Lotko, W., Brambles, O. J., Wang, W., Lei, J., Wiltberger, M., et al. (2015). Pathways of *F* region thermospheric mass density enhancement via soft electron precipitation. *Journal of Geophysical Research: Space Physics*, *120*, 5824–5831. https://doi.org/10.1002/2015JA020999

Erratum

In the originally published version of this article, there was a minor error in the abstract. The last characters of the abstract, "nW/m^2" were changed to "nW/m^3". This version may be considered the authoritative version of record.